Materials Science-Poland, 41(1), 2023, pp. 124-139
http://www.materialsscience.pwr.wroc.pl/
DOI: 10.2478/msp-2023-0005

Effect of heat treatment and cooling rate on microstructure and properties of T92 welded joint

Chengyong Ma[1], Zhiquan Wu[2], Yanchang Qi[1], Xin Zhang[3,*]

[1]Welding Institute, Ceneral Iron and Steel Research Institute, Beijing 100081, China
[2]SPIC Yunnan International Power Investment Co., Ltd., Kunming 650228, China
[3]Institute of New Energy Technology, State Power Investment Corporation Research Institute, Co. Ltd., Beijing 102206, China

The effects of heat treatment and cooling rate on the microstructure and properties of T92 welded joints were studied. Under the same tempering holding time, the diffusion ability in the deposited metal increased as the tempering temperature increased. The phase-change temperature was lower than the A_{C1} points. In the 5-20s range of $t_{8/5}$, the deposited metal toughness decreased as the cooling rate increased. When the $t_{8/5}$ was equal to 70s, the toughness increased and the hardness decreased. The higher heat input induced coarse grain tendency. The lower welding heat input should be used in conjunction with the reasonable post-weld heat treatment.

Keywords: *T92 welded joint, microstructure, heat treatment, cooling rate*

1. Introduction

In order to improve the power efficiency of power plants, the reduction of CO_2 emissions and the consumption of a high amount of fuel, all countries in the world developed the turbine inlet steam parameters of supercritical and ultra-supercritical units with higher temperature (600°C) and pressure (beyond 31MPa) [1, 2]. The development of materials with long service life under high temperature and high pressure has become the key to the development of supercritical and ultra-supercritical units. With the constant construction of high parameter and high capacity units, the new heat-resistant steel has been widely utilized in the new units. At present, a wide range of new heat-resistant steels, mainly the ferritic heat-resistant steels such as T91, P91, T92, P92, T122, and P122 exist, as well as austenitic heat-resistant steels, such as the Super304H, TP347HFG, and HR3C [3, 4]. In addition, Cr, W, Cb, and other alloying elements have been added to the new heat-resistant steel, while the high-temperature creep rupture strength of the material was improved, such as for the V martensitic heat-resistant steel [5–7]. In addition, the content of C in the T92 steel is low, while the relative F12 as well as other steels have good welding properties. Therefore, significant amounts of T92 steels have been utilized in the high-temperature superheater and ultra-supercritical units in the high-temperature re-heater, the super-heater, and other components.

When the T92 was welded, the impact toughness of welded joints is proved lower compared to the base metal, which constitutes a prominent problem encountered in the T92 steel application. Due to the T92 steel toughness reduction subsequent to aging, the heat treatment is an effective method to improve the toughness of welded joints. In the production line of Mitsubishi Co. in Japan, [8] a small amount of rare earths was added in the TIG welding wire, for element control with w (Mo)/3 +w (W)/2 +w (RE)=0.5%, which improved the welding joint creep strength; the toughness was also significantly improved. This was attributed to the rare earth oxides' ability to improve the crystal structure. The rare earth weakened the direction of the columnar crystal, shortening the crystal column, improving the health organization at the fusion line, while the rare earths also strongly affected the morphology

* E-mail: kmzx201@163.com

© C. Ma et al. 2023. This is an open access article distributed under the Creative Commons Attribution-NonCommercial-NoDerivatives 4.0 License. (http://creativecommons.org/licenses/by-nc-nd/4.0/)

and distribution of carbides in the weld. In the Kobelco company of Japan [9], niobium and vanadium were added, with strong carbide forming elements for arc welding, while both element quantities were adjusted along with the total carbon content ratio, which could inhibit the migration of the produced carbide and side plate ferrite. American Electric Power Research Institute controlled the content ratio of niobium and carbon to suppress the carbon content ratio in the welding wire, and the carbon migration of the ferrite steel dissimilar joint could be suppressed [10]. Also, the service life of the welded joint was prolonged. Niobium and vanadium are also the elements that reduce toughness, which reduced the welded joint toughness. Kobelco suggested that niobium and vanadium in the flux cored wire could increase the toughness of the welded joint [11].

The impact toughness of the welded joint was quite a bit lower compared to the base metal during welding, which constituted a severe problem for the T92 steel application [12]. Aging treatment is an effective way to maintain toughness for the T92 steel welded joints. The toughness of these welded joints has not been substantially improved, although a great deal of research has been carried out, in aspects of welding materials, welding technology, and post-weld heat treatment. Due to the urgent demand for ultra-supercritical plants at present, most of the research was focused on the T92 steel engineering applications field since its development. Besides, the investigations on welding materials and welding technology have been limited in meeting the minimum requirements of the ASME standard for similar steels [13]. Consequently, a systematic study was necessary to discuss the substantial reasons for low welded joint impact toughness.

Work that clarifies the welded joint mechanism for lower impact toughness and the effects of heat treatment and cooling rate on the microstructure and properties of the welds for the T92 steel would be of significant guidance to the development of T92 steel welding materials, as well as for the welding technology.

2. Materials and methods

2.1. Experimental materials

2.1.1. Materials

The welding wires for testing were developed. Welding wire diameter was 1.6 mm. The actual compositions of the welding wires and the deposited metal were determined through the Inductively Coupled Plasma-Atomic Emission Spectrometry analysis, and the results are presented in Table 1 and Table 2. The impurity contents of S, P, and O in all three welding wire types were below 0.005 wt.%.

2.1.2. Test specimen

The V belt plate groove was adopted as the welding plate to weld the deposited metal. The test plate material was a T92 steel plate of 250×150×20 mm. The schematic diagram of the V groove was presented in Figure 1. In order to prevent the dilution effect of the welding wire deposited metal component during gas protection welding, the same testing welding wires were utilized for the isolation layer on both sides to acquire a surfacing thickness of approximately 8mm and for the TIG backing weld at the groove bottom.

The AMET Manipulator welding machine with the TIG automatic welding system was utilized to perform the pulsed TIG welding on the test plate. The shielding gas was 100% argon, and the gas flow was 15 L/min. Table 3 presents the welding parameters. The first five beads were the backing welds. The interpass temperature and wire feed rate were modified, to maintain the interpass temperature range within 150–200°C.

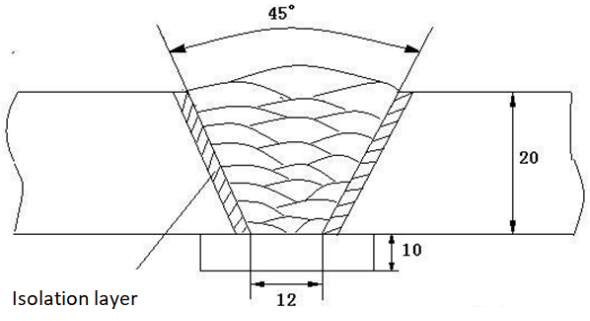

Fig. 1. Schematic diagram of multi-layer welding

Table 1. The chemical composition of welding wires (wt%)

C	Mn	Nb	B	Ni	Cr	N	Si	Mo	W	V
0.100	0.890	0.0350	0.003	0.680	8.790	0.073	0.220	0.780	1.570	0.200

Table 2. The chemical composition of deposited metal (wt%)

C	Mn	Nb	B	Ni	Cr	N	Si	Mo	W	V
0.099	1.010	0.033	0.004	0.660	8.338	0.070	0.180	0.68	1.310	0.170

Table 3. Welding parameters

Welding Beads	Welding current /A	Welding voltage /V	Welding speed /(cm·min^{-1})	Interlayer temperature /°C	Heat input /KJ/cm
1	250	12	14	25	12.86
2	250	12	14	96	12.86
3	250	12	14	170	12.86
4	250	12	14	226	12.86
5	250	12	14	240	12.86
6	250	12	14	190	12.86
7	250	12	14	190	12.86
8	250	12	14	190	12.86
–	–	–	–	–	–
28	250	12	14	190	12.86
29	250	12	14	190	12.86
30	250	12	14	190	12.86

2.2. Experimental methods

2.2.1. Mechanical properties of deposited metal

According to GBT 229-2007 Metallic Materials Charpy Pendulum Impact Test Method, the Charpy shaped notch (V Notch V) test was utilized to measure the impact toughness of the material through single pendulum impact tests, and the performance index was the impact energy absorption. From the tensile tests, the mechanical properties could be obtained, including the yield strength ($R_{P0.2}$), the tensile strength (R_m), the elongation subsequently to fracture (A%) and the reduction of area (Z%). Figure 2 presents the deposited metal impact location and the tensile specimens. The impact tests were performed with the JBN-300 test machine at high temperatures (740°C, 760°C, and 800°C).

Figure 3 presents the sketch map of the tensile testing samples. The tensile specimens were manufactured as round bar specimens of $\Phi 6 \times 105$ mm in standard size. The tensile tests were performed with the UH-F50A (250 kN) test machine at high temperature (740°C, 760°C, and 800°C). The surface weld pass hardness of the deposited metal was tested by the FM-300 FUTURE-TECH automatic micro hardness tester. The load and load time were 5000 g and 10 s, respectively.

2.2.2. Investigation on microstructure and fracture of deposited metal

The spark emission spectrometer was utilized to analyze the composition of the deposited metal. The specimens for metallographic observations were cut along the longitudinal direction of the weld pass. Applied subsequent to grinding and polishing, the etching solution was 1 g picric acid + 100 ml alcohol + 5 ml hydrochloric acid, and the corrosion time was 30 s. Following this, the deposited metal microstructure was investigated with the MEF-4M metallographic microscope and the SCIAS 6.0 image analysis system. The second phases and the impact fracture surfaces of the deposited metals were analyzed with the HITACHI S-

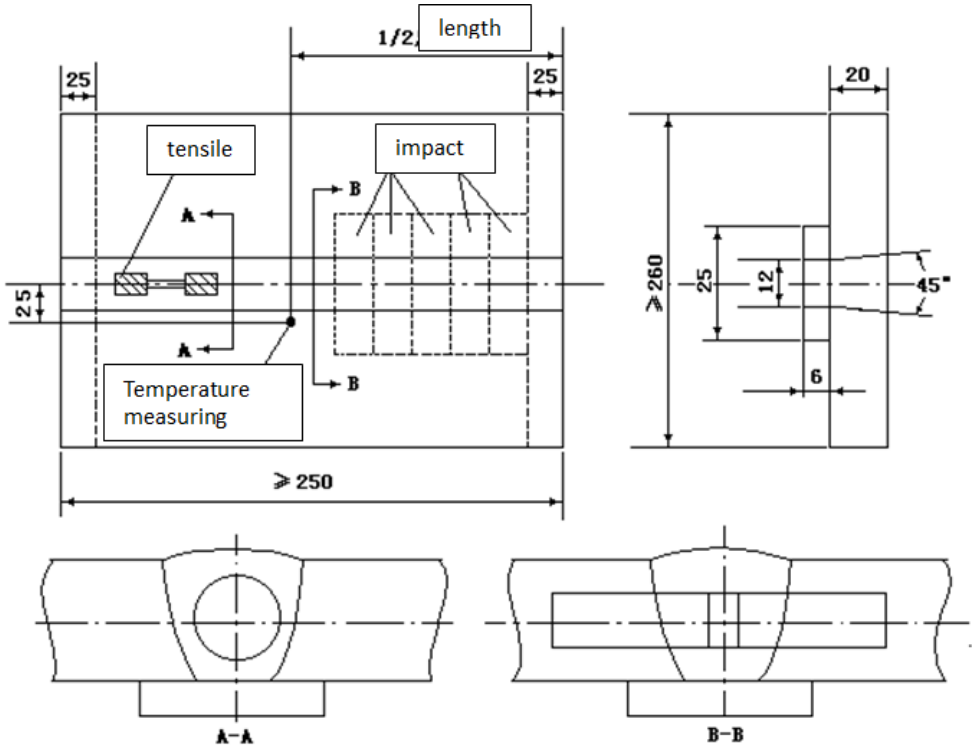

Fig. 2. Location of deposited metal impact and tensile specimens

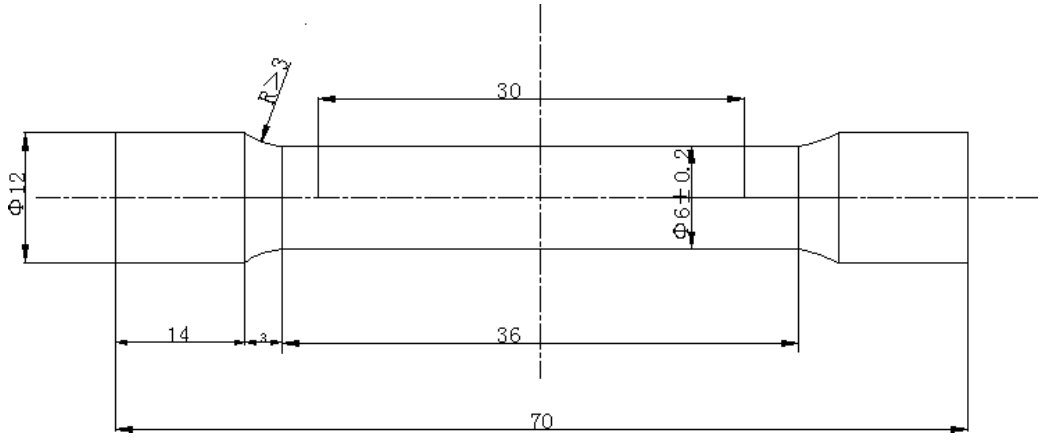

Fig. 3. Sketch map of tensile samples processing

4300 Scanning Electron Microscope equipped with a matching Energy Dispersive Spectrometer. The Transmission Electron Microscope H-800 was selected for the fine structure and qualitative analysis investigations in the second phase.

2.2.3. Thermal expansion tests

The transformation points (A_{c1} is called a eutectoid line, A_{c3} is the final temperature at which ferrite is transformed into austenite during heating) of the weld metal were measured with the Fuji FORMASTER-DIGITAL thermal dilatometer. The heating speed was 200°C/h, and the heating temperature of the experimental procedure was ap-

proximately 1000°C. After holding the heated samples for 10 s, the helium was utilized to control cooling. Subsequently, to sample complete annealing, the sample was as shown in Figure 4. According to the phase change point temperature, the heat treatment was as follows: the temperatures of 740°C, 760°C, and 800°C were selected as the heat preservation temperatures; the holding times of every deposited metal were 2 h, 4 h, and 8 h. The effects of temperature and holding time on the properties of weld metal were studied, respectively.

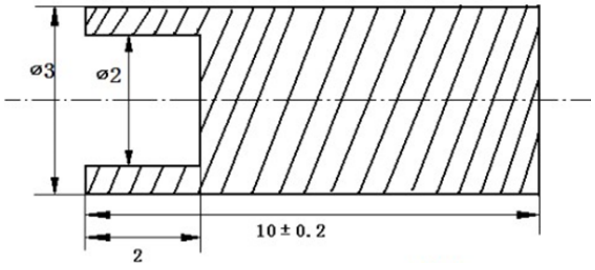

Fig. 4. Size of thermal expansion sample

The thermal simulation test was conducted with the Gleeble-1500 thermal simulation test machine. The maximum heating peak temperature (T_{max}) was = 1350°C. The samples were cut into 10.5 mm×10.5 mm×61 mm segments. The samples were designed with four types of cooling rate and the $t_{8/5}$ (that is, cooling time from 800°C to 500°C) of 5, 10, 20, and 70 seconds were utilized.

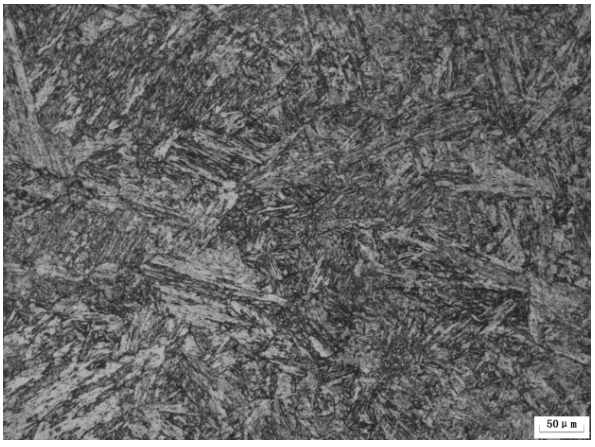

(A)

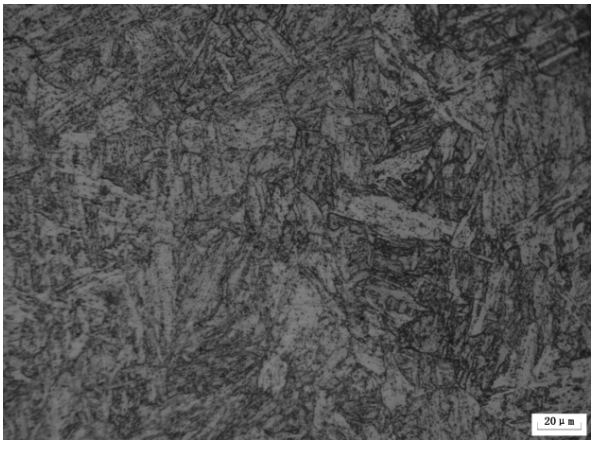

(B)

Fig. 5. Deposited metal microstructure: a-50 μm, b-20 μm

3. Results and Discussion

3.1. Microstructure of deposited metal

The mixed corrosion liquid could lead to the martensite color becoming darker than the ferrite coloring. Figure 5 presents the deposited metal microstructure. It can be observed from Figure 5 that the tempering microstructure of the deposited metal microstructure was uniform. The microstructure of martensite in the weld metal was relatively clear. A high amount of martensite lath presented which was consistent with the crystalline direction.

The phase change points A_{c1} and A_{c3} of the deposited materials were 773°C and 850°C, as measured through thermal expansion testing. The sample heat treatment holding temperatures were 740°C and 760°C, which were below the A_{c1} point. The heat treatment holding temperature was 800°C, which was between A_{c1} and A_{C3}. Figures 6, 7, and 8 present the typical metallurgical structures of the deposited metal under various holding temperatures and times. Following lapping and polishing, the deposited metal was corroded with a mixed solution of 5 g $CuCl_2$, 30 ml HCl, 25 ml alcohol, and 30 ml H_2O. The ferrite was colored, and the martensite color became deep. It can be observed in Figure 6 that the tempering time of 2 h could not guarantee the sufficient tempering of the deposited metal. Due to the lower temperatures, the incompletely tempered martensite structure existed in the

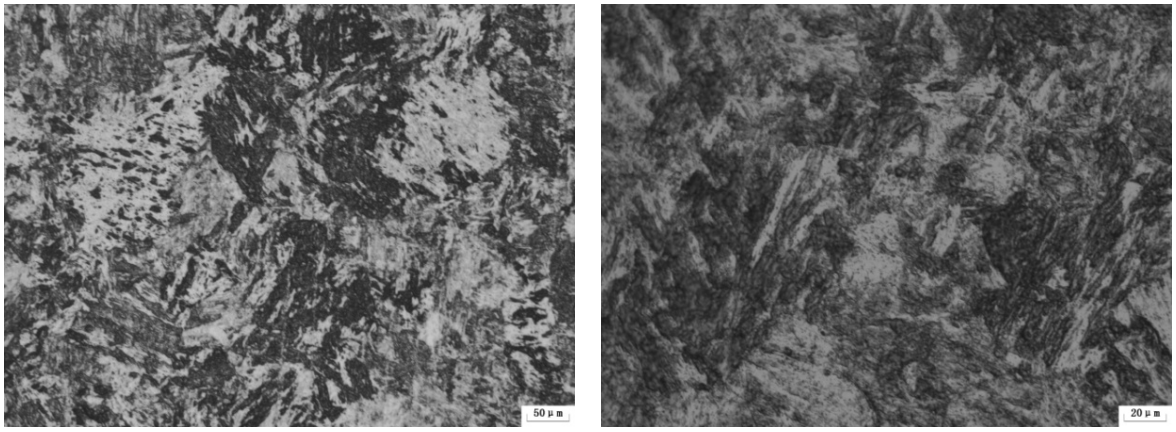

(A)

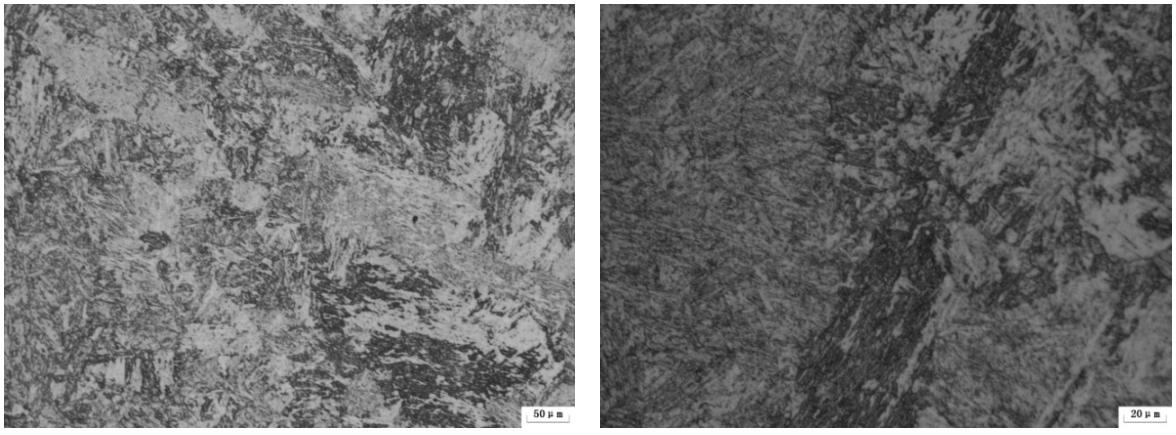

(B)

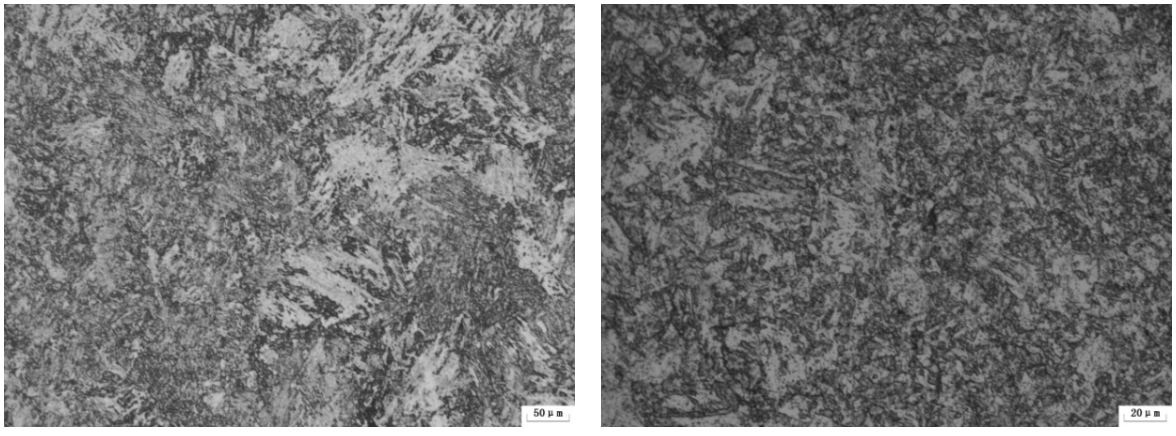

(C)

Fig. 6. Holding temperature of heat treatment at 740°C: (a) 2 h, (b) 4 h, (c) 8 h

deposited metals, such as the black area in Figure 6a. The room temperature microstructure was composed of tempered martensite, non-tempered martensite, and the second phase formed during tempering. As the tempering time increased, the tempering microstructure of the deposited metal became uniform. Its microstructure at room temperature was a single-tempered martensite and the

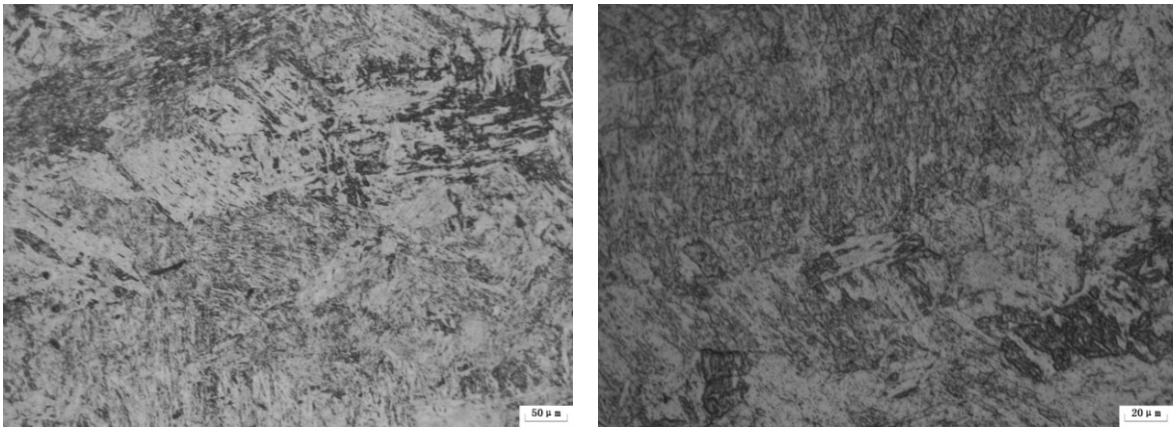

(A)

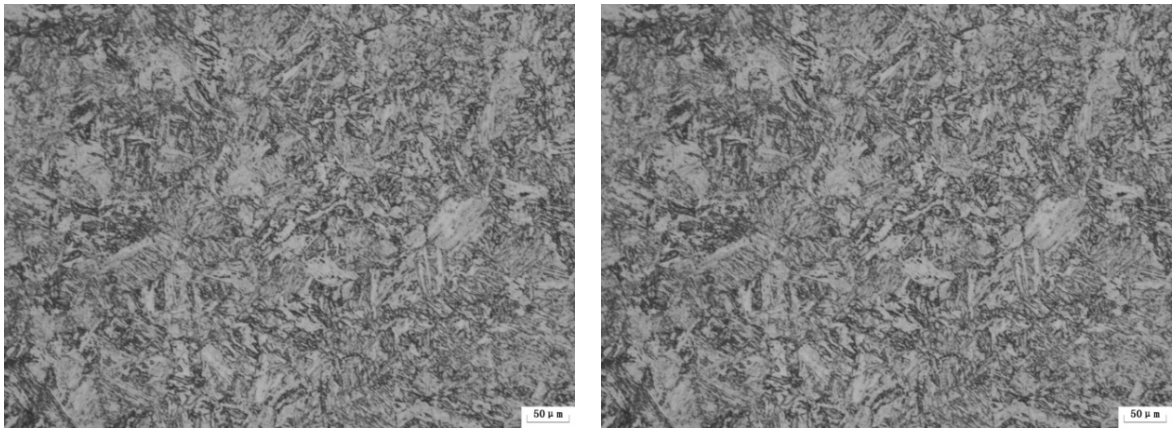

(B)

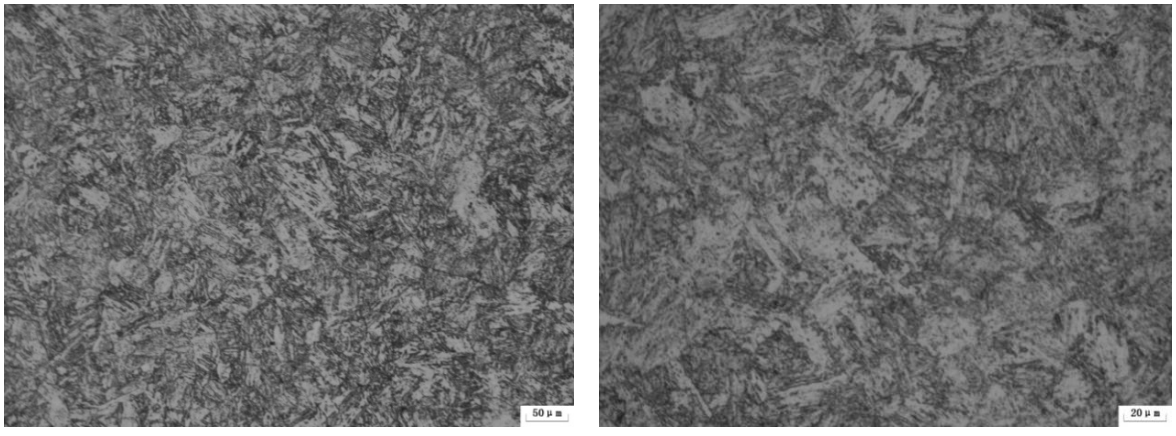

(C)

Fig. 7. Holding temperature of heat treatment at 760°C: (a) 2 h, (b) 4 h, (c) 8 h

uniformly distributed second phase [14].

As seen in Figure 7, as the heat treatment temperature increased, the tempering microstructure time of the deposited metal to reach the uniformity time decreased. This meant that the tempering at low temperature required a longer time to temper the homogenized structure, while the required tempering time decreased accordingly as the tempering

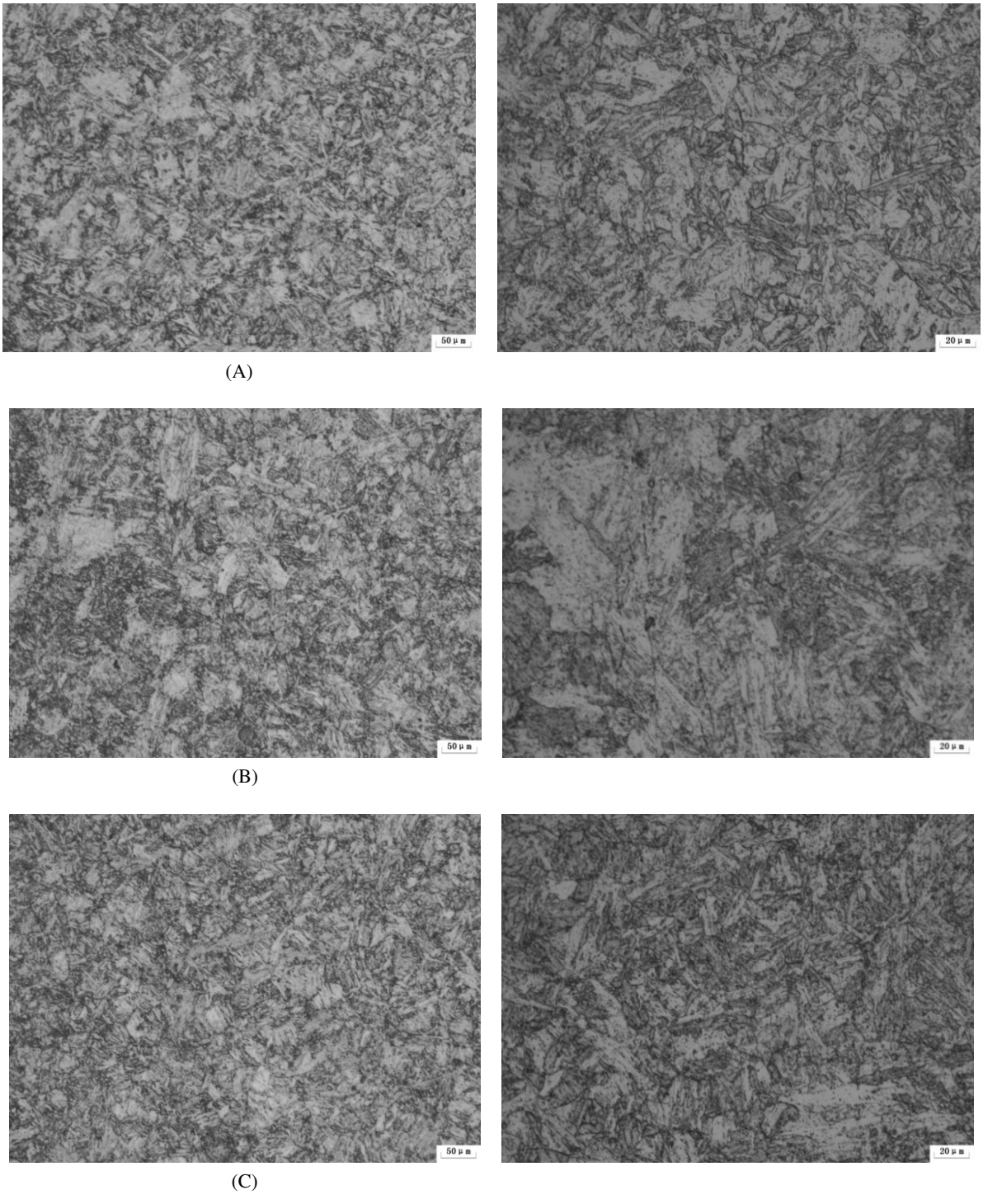

Fig. 8. Holding temperature of heat treatment at 800°C: (a) 2 h, (b) 4 h, (c) 8 h

temperature increased. As can be observed in Figure 8, the martensite lath began to decompose when the tempering temperature was 800°C. Simultaneously, the segregation and dissolution of the carbonitride decreased the deposited metal strength.

The tempering-induced fine dispersed second phases precipitated in the deposited metal. The second phase precipitated with unequal size distribu-

tion in the original austenite grain boundaries, as well as in the lath bundle boundaries and in the crystal. However, the partition of the non-tempered precipitated phases was small. Figure 9 presents the distribution of the second phases in the tempered and non-tempered martensite microstructure. It can be seen in Figure 9 that dispersed fine second-phase precipitates existed in the tempering zone of martensite, while the second phase was mainly composed of the $M_{23}C_6$ and MX phases. The carbonitrides in the non-tempering zone (black areas in Figure 6) were the solid solution treatment phases.

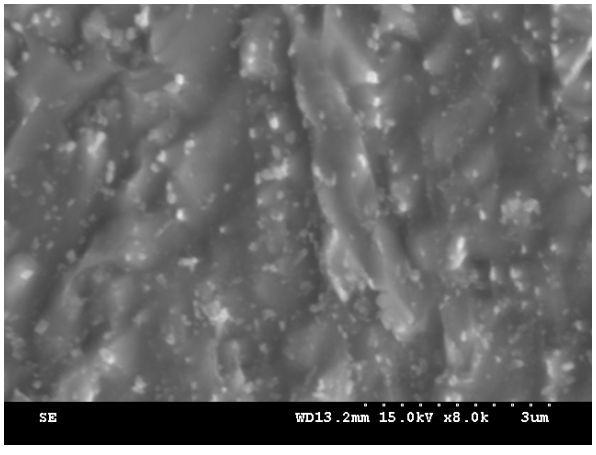

(A)

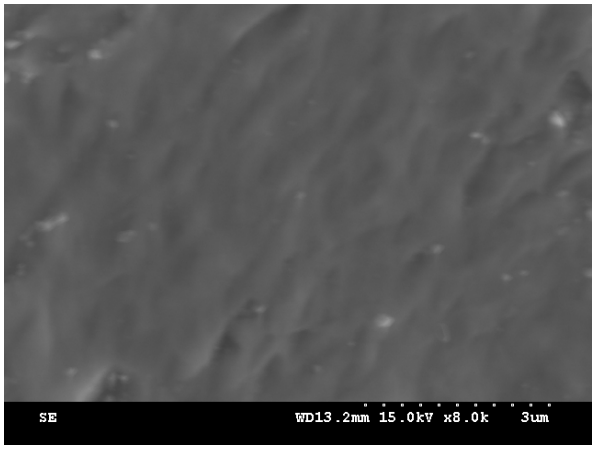

(B)

Fig. 9. Second phase of deposited metal: (a) Tempering area, (b) Non-tempering area

3.2. Mechanical properties of different heat treatment processes

Figure 10 presents the impact absorption work of different tempering temperatures and holding times. With the increase of heat treatment temperature, the toughness of the same deposited metal increases, obviously. With the decrease of heat treatment temperature, the average impact toughness shows an increasing trend, but the increasing trend slows down gradually. At the same temperature, with the increase of time, the impact energy at the three temperatures shows three obviously different trends. At low temperature, it increases slowly and then rapidly. The change trend is not obvious at medium temperature. At high temperature, it shows a gradual increasing trend.

The toughness value of the deposited metal after heat insulation for 2 h at 760°C was equal to the toughness value after heat insulation for 8 h at 740°C.

It could be observed that the heat treatment temperature increase could improve the working efficiency. The excess temperature in heat treatment was also unfavorable. However, the excess temperature in heat treatment could increase the weld metal toughness and severely favor the martensite decomposition. The carbonitrides segregation in the deposited metal highly reduced the weld metal strength. The aging temperature of the deposited metal must be strictly controlled to ensure the high temperature strength of the deposited metal.

The deposited metal hardness under different heat treatments was measured through the Vickers hardness measurement, and the load was 5000 g. For each heat treatment process, the hardness of the deposited metal sample is shown in Figure 11. The hardness acquired from different heat treatment processes had a certain corresponding relationship with toughness. With the increase of heat treatment temperature, the hardness of the same deposited metal is obviously reduced. With the decrease of heat treatment temperature, the decrease of hardness value is more obvious. When the temperature is reduced to a certain extent, the decrease of the hardness value is no longer obvious.

Table 4. Fiber fracture rate of deposited metals

Tempering temperature (°C)	Holding time (h)	Fiber fracture rate /%		
		$T = 2$h	$T = 4$h	$T = 8$h
740	Measured value	20; 22; 24	36; 37; 41	82; 83; 86
	Average value	22	38	84
760	Measured value	35; 35; 43	52; 54; 51	48; 55; 50
	Average value	84	86	89
780	Measured value	86; 84; 88	87; 85; 86	89; 88; 85
	Average value	86	86	87

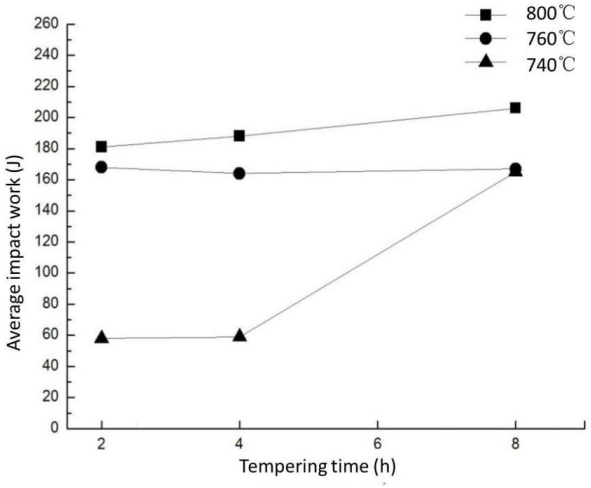

Fig. 10. Average impact toughness of deposited metal-heat treatment curves

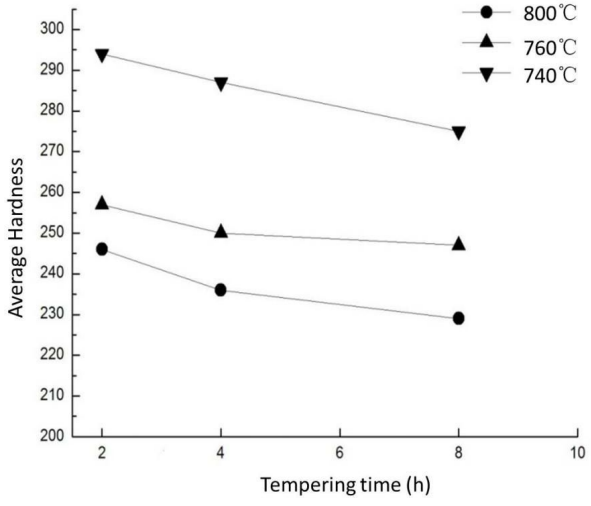

Fig. 11. Average hardness of deposited metal-heat treatment curves

3.3. Analysis of fracture surface under different heat treatments

The impact fracture of the deposited metal under different heat treatment processes was measured and the results are presented in Table 4 and Figure 12. It could be observed that the lower the fibrous fracture rate was, the higher the brittleness tendency was, as well as the higher the toughness was and the better the average value was. The fibrous area proportion had a good correspondence with the impact work height, while its fibrous fracture rate increased as both the heat treatment temperature and the holding time increased. Under the condition of 740°C tempering temperature, the fibrous fracture rate was below 40% and the brittleness tendency was quite severe, when the samples were heat treated for at least 2 h and approx-

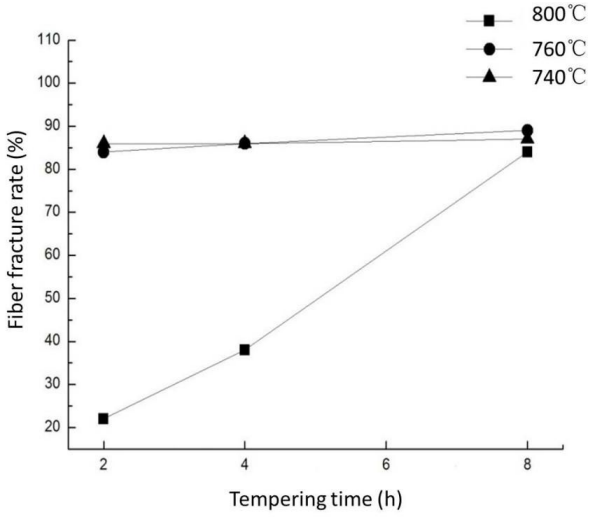

Fig. 12. Fiber fracture rate of deposited metals-heat treatment curve

imately 4 h. When the holding time increased to 8 h, the toughness apparently increased. At the tempering temperature of 760°C and 800°C, the fiber fracture rate changed slightly. It could be observed that under the tempering temperature of 760°C and 800°C, the toughness increase was not apparent as the holding time increased.

Figures 13, 14, and 15 show the impact fracture morphologies of each heat treatment process. Under different heat treatment conditions, the impact fracture was composed of three zones: the fiber zone, the radiation zone, and the shear lip zone. Due to the differences in fracture properties and impact absorption work values, the proportion of each region differed. As can be seen, under the tempering temperature of 740°C, the proportion of the radiation zone in the impact fracture of the thermal insulation for 2 h and 4 h reached beyond 80% and 60%, respectively, which was attributed to brittle fracture. As can be seen in Figure 13a and 13b, the fracture patterns were mainly river and scallop patterns, accompanied by a torn edge. The fracture mechanism was quasi-cleavage transgranular. When the holding time increased to 8 h, the proportion of fiber area reached beyond 80%, while the fracture mechanism changed from the quasi-cleavage fracture to the ductile fracture. The fracture morphology, presented in Figure 13c, was mainly dimple morphology. It could be observed from Figures 14 and 15 that the fiber fracture rate exceeded 80%, at the tempering temperature of 760°C, while the ductile fracture mode was mainly manifested as dimple type.

3.4. Effect of $t_{8/5}$ cooling rate on microstructure and properties of welds

Figure 16 presents the metallographic structure of the weld, when the simulated $t_{8/5}$ times were 5 s, 10 s, 20 s, and 70 s. The heat treatment was not considered on the simulated welded joints. The corrosion solution mixed with 5 g $FeCl_3$, 15 ml HCI, and 80 ml H_2O was utilized to corrode the microstructure of the deposited metal. As can be observed in Figure 16, the organizations were all martensite tissues, when the simulated $t_{8/5}$ cooling rate changed from 5 s to 70 s, which demonstrated that the weld

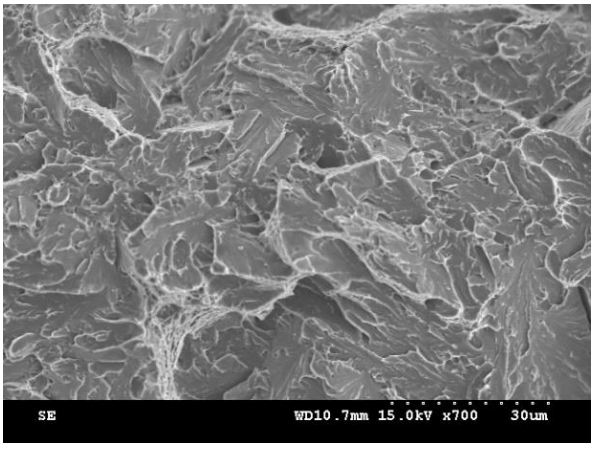

(A)

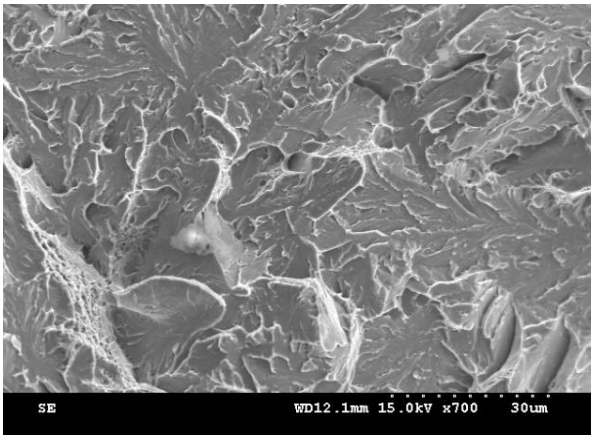

(B)

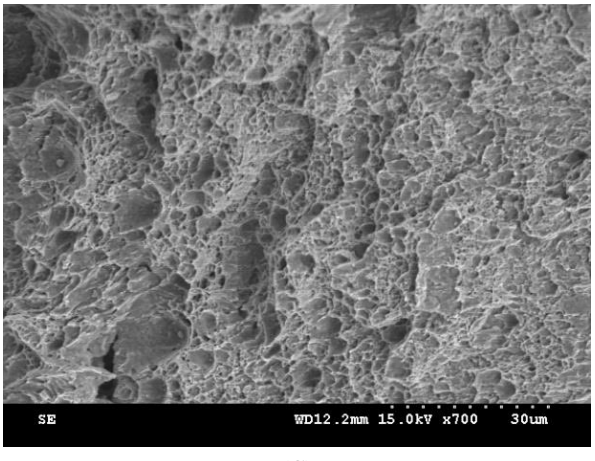

(C)

Fig. 13. Impact fracture morphology at tempered 740°C: (a) 2 h, (b) 4 h, (c) 8 h

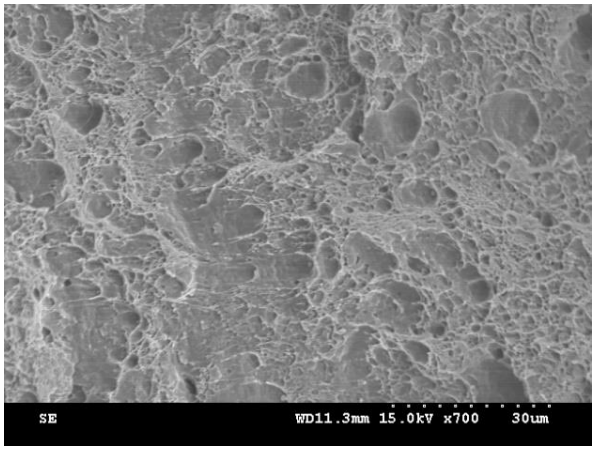

(A)

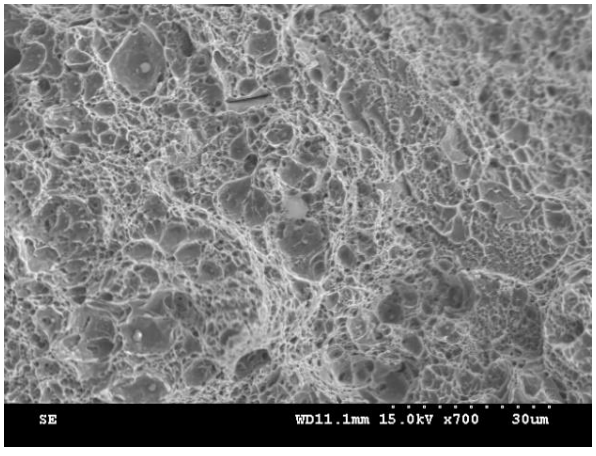

(B)

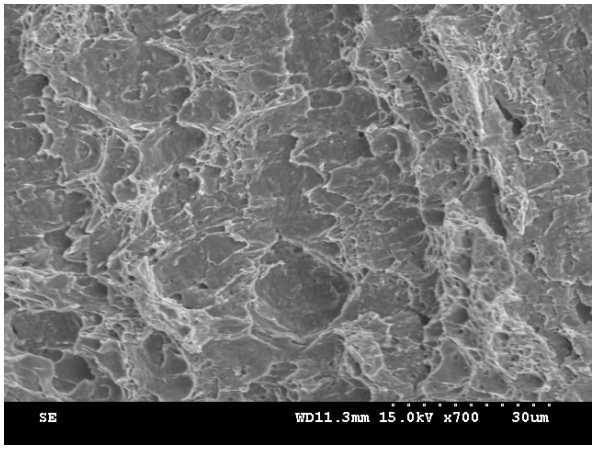

(C)

Fig. 14. Impact fracture morphology at tempered 760°C: (a) 2 h, (b) 4 h, (c) 8 h

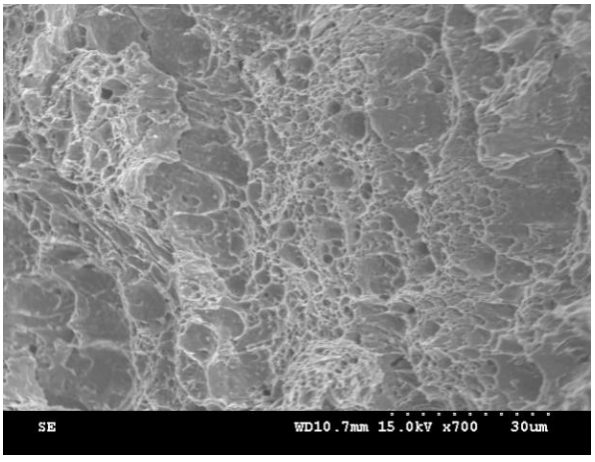

(A)

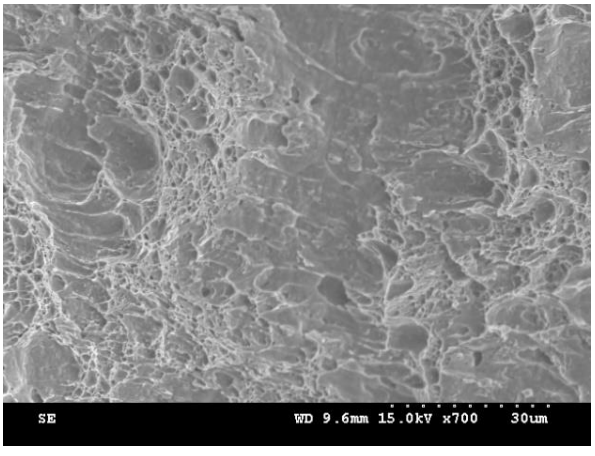

(B)

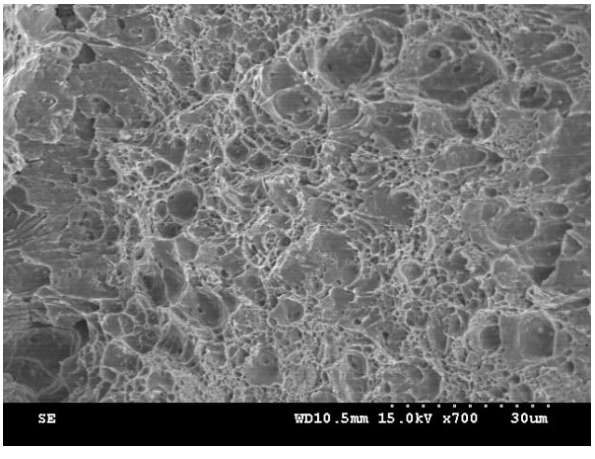

(C)

Fig. 15. Impact fracture morphology at tempered 800°C: (a) 2 h, (b) 4 h, (c) 8 h

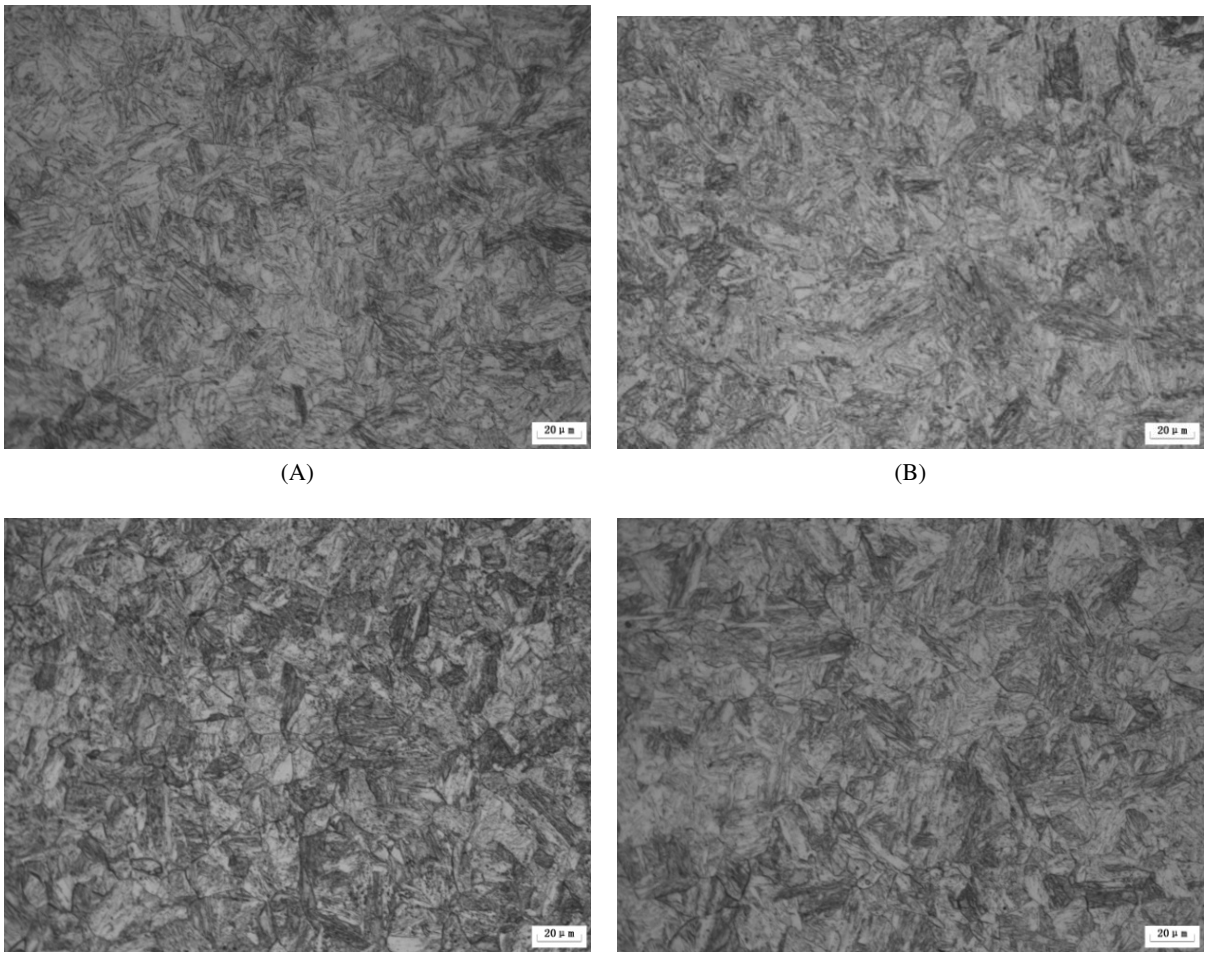

(A) (B)

(C) (D)

Fig. 16. Microstructure morphology of weld simulation $t_{8/5}$: (a) 5 s, (b) 10 s, (c) 20 s, (d) 70 s

metal could obtain a martensitic structure under a wide heat input. Generally, as the welding heat input increased, the grains would become coarse, the toughness would decreased, and the hardness would increase.

The curves of toughness and hardness with the $t_{8/5}$ cooling time are presented in Figures 17 and 18, respectively. It can be observed that when the $t_{8/5}$ was lower than or equal to 20 s, the toughness of the weld joint decreased as the $t_{8/5}$ increased. However, the weld toughness substantially increased when the $t_{8/5}$ reached up to 70 s. The trend of hardness variety was more consistent with the trend of toughness variety. When the $t_{8/5}$ was lower than or equal to 20 s, the hardness increased, while the weld hardness decreased significantly at $t_{8/5}$=70 s. The occurrence of this phenomenon and the Precipitation Law of the second phase in the weld had a certain relation to the welding heat input change. The dissolution and precipitation of the second phase in the iron matrix was a reversible chemical reaction process [15]. The number of elements involved in the second phase in a solid solution matrix and the amount present in the second phase tend to be balanced subsequently to prolonged temperature preservation. The temperature change under certain chemical compositions of the steel, the amount of solid solution, and the content of the second phase will also change [16].

The main secondary phase precipitation strengthening phases in the T92 steel were the

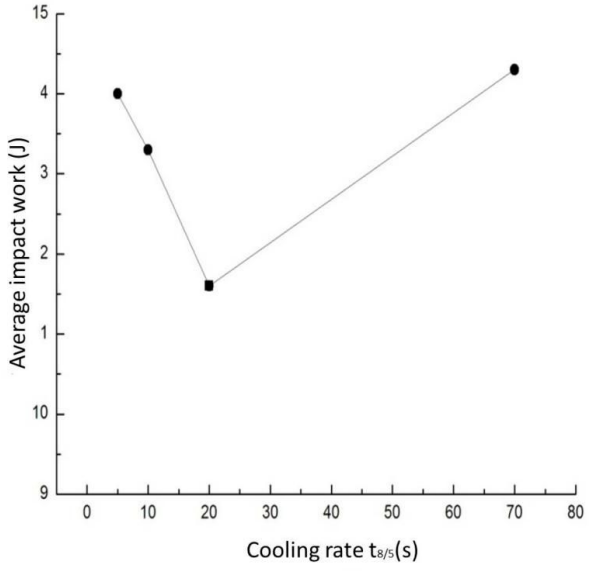

Fig. 17. Relationship between impact toughness of weld and $t_{8/5}$

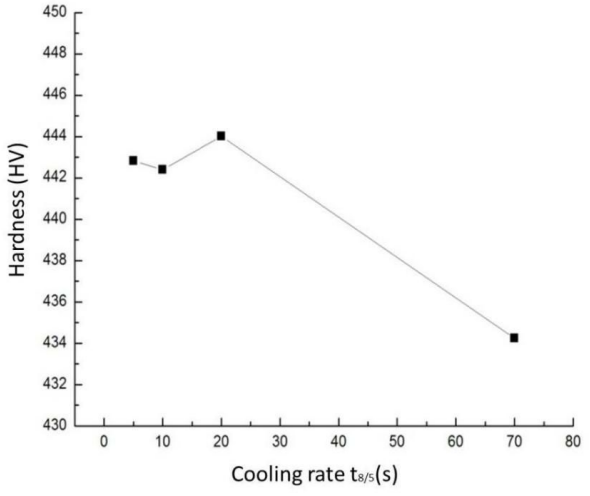

Fig. 18. Relationship between hardness of weld and $t_{8/5}$

$M_{23}C_6$ and MX phases, and the stable MX phase (M=V, Nb; X=C, N) was mainly distributed within the sub-grain, while the $M_{23}C_6$ phase enriched in Cr mainly precipitated at the grain and sub-grain boundaries. The MX phase was relatively stable, while the low growth rates of the MX phases maintained even at high temperature for a long time, which played an important role in the high temperature strength durability of the T/P92 steel. In contrast, the $M_{23}C_6$ growth under high temperature was apparent, while B was added to restrain the $M_{23}C_6$ growth rate at high temperature. In addition, the T/P92 steel would produce a brittle Laves phase at high temperature for a long tempering time, which precipitated along the original austenite grain boundaries, the martensite blocks, and the lath boundaries [17]. The effect of the Laves phases on the high-temperature performance of the T/P92 steel depends on their distribution and size. When the coarsening rate of the Laves phase is low, it has a beneficial effect on the high-temperature creep strength improvement. When the high-temperature aging and creep deformation increased in duration, the coarsening rate would increase, while the relative creep strength effect of the Laves phases would change to the harmful [18]. For the aforementioned three types of main precipitates in the welding cooling process, the precipitation of the $M_{23}C_6$ and MX phase contents increased as the temperature decreased under the equilibrium state, as presented in Figure 16b. The welding cooling process was a non-equilibrium state. When the cooling rate was higher, the precipitation of the second phases were inhibited, while most second phases became solid-solutes in the matrix. When the cooling rate was lower, the precipitation time of the second phase was longer and the amount of precipitation was relatively higher.

In Figure 16, when the $t_{8/5}$ was lower than or equal to 20 s, the cooling rate increased, the second phase precipitation was inhibited, so the second phase could be ignored. As the heat input increased, the toughness decreased, and the hardness increased. When the $t_{8/5}$ was equal to 70 s, the second phase of precipitation was relatively increased in amount and the role of second phases in the matrix had the following two points [19]. Firstly, the C and N interstitial solution strengthening elements with relatively high brittleness vector would precipitate in the relatively low-sized MX phase of the brittle medium, which reduced the matrix stress. Secondly, the precipitated second phase had the grain boundaries pinning role, which could inhibit the grain growth and alleviate the heat input caused by the grain growth to a certain extent. Therefore, these two points would present the rebound phe-

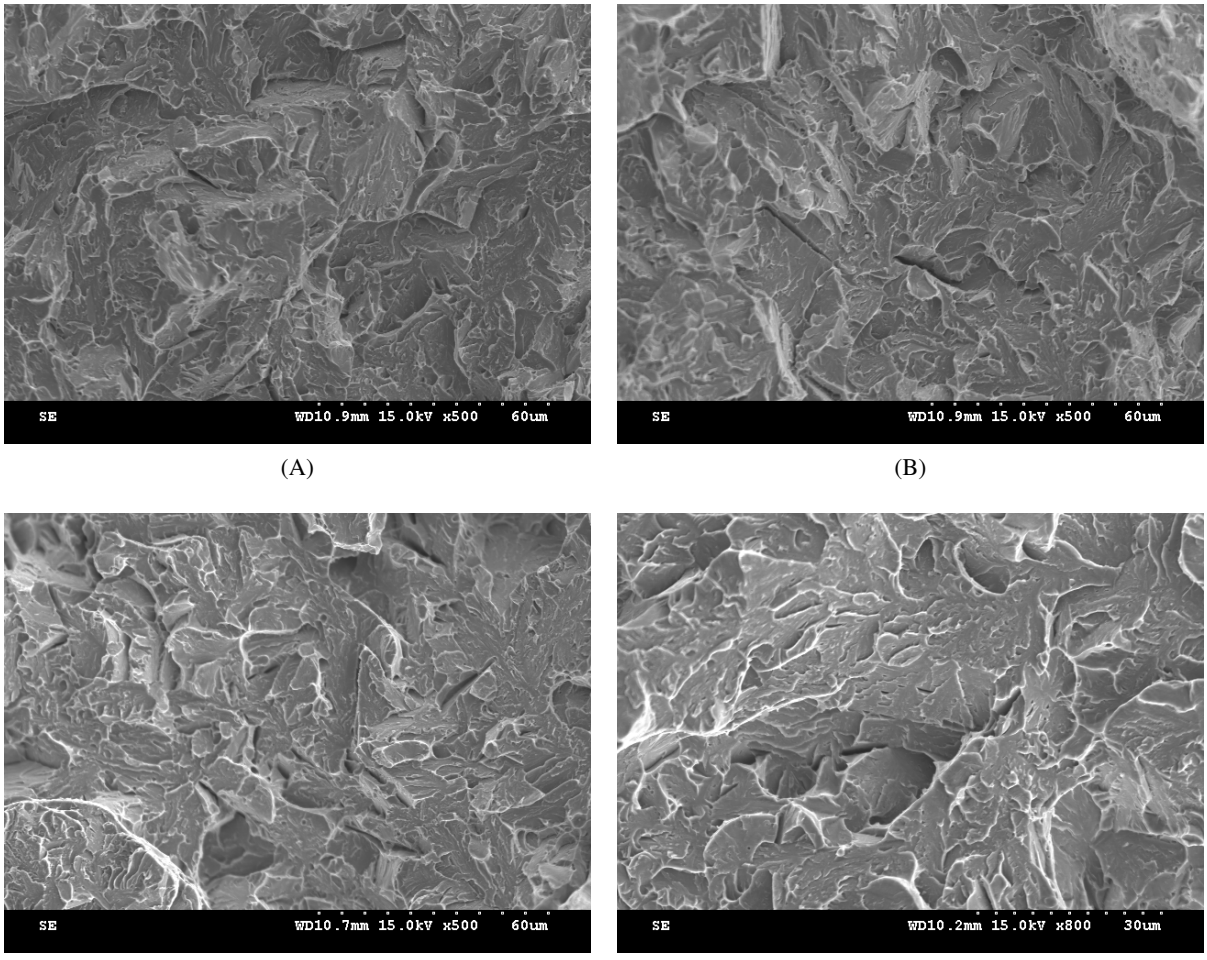

(A) (B)

(C) (D)

Fig. 19. Impact fracture morphology of thermal simulation $t_{8/5}$: (a) 5 s, (b) 10 s, (c) 20 s, (d) 70 s

nomenon of toughness, while the hardness value decreased when the $t_{8/5}$ was equal to 70 s.

Figure 19 presented the fracture at different cooling speeds. The fracture was composed of the cleavage fracture mode under the different cooling rates in the thermal simulation state, which was mainly related to the welding joints without heat treatment subsequent to welding. The C and N interstitial solution strengthening elements with relatively high brittleness vector and the forming elements of strong and medium carbon nitrides almost completely dissolved in the matrix in the state of the solid solution under the faster cooling rate following a thermal simulation, while the fracture modes were brittle fractures.

4. Conclusions

1. The higher tempering temperature could promote the precipitation completion of the second phase, the toughness improvement, as well as the microstructure homogenization of the T92 deposited metal in a short time. The extremely high tempering temperature would lead to the severe decomposition of the martensite phases, while the carbon-nitride compounds presented severe segregation and growth.
2. The tempering temperature of the deposited metal should not exceed the A_{C1} points of the T92 steel. Higher welding heat input can

easily cause the grain coarsening of the deposited metal.

3. Within the range of 5–20 s, the deposited metal toughness decreased as the $t_{8/5}$ increased. When the $t_{8/5}$ was equal to 70 s, the toughness increased, and the hardness decreased.
4. The lower welding heat input should be used in conjunction with the reasonable post weld heat treatment system.

References

[1] Viswanathan R, Henry JF, Tanzosh J, Stanko G, Shingledecker J, Vitalis B, Purgert R. U.S. program on materials technology for ultra-supercritical coal power plants[J]. *J. Mater. Eng. Perform.*, 2005, 14(3):281-292..DOI: 10.1361/10599490524039.

[2] Li S, Hu L, Dai PY, Bi T, Deng D. Influence of the groove shape on welding residual stresses in P92/SUS304 dissimilar metal butt-welded joints. *J Manuf Process*, 2021, 66: 376-386. DOI: 10.1016/j.jmapro.2021.04.030.

[3] Viswanathan R, Sarver J, Tanzosh JM. Boiler materials for ultra-supercritical coal power plants—Steamside oxidation[J]. *J. Mater. Eng. Perform.*, 2006, 15(3):255-274. DOI:10.1361/105994906X108756.

[4] Dai Z, Qi YC, Zhang X, Wu ZQ, Ma CY, Yin Q. Microstructure and properties of multipass and wire welded joints on Super304H steel. *Mater Lett*, 2020, 270: 127698. DOI: 10.1016/j.matlet.2020.127698.

[5] Ennis PJ, Czyrska-Filemonowicz A. Recent advances in creep resistant steels for power plant applications. *Sadhana*, 2003, 28(3): 709-730. DOI: 10.1007/BF02706455.

[6] Tan SP, Wang ZH, Cheng SC, Liu ZD, Han JC, Fu WT. Hot deformation behavior of Super304H austenitic heat-resistant steel. *Int J Miner Metall Mater*, 2010, 17(2): 167-172. DOI: CNKI:SUN:BJKY.0.2010-02-009.

[7] Dak G, Pandey C. Experimental investigation on microstructure, mechanical properties, and residual stresses of dissimilar welded joint of martensitic P92 and AISI 304L austenitic stainless steel. *Int J Press Ves Pip*, 2021, 194(Part A): 104536. DOI: 10.1016/j.ijpvp.2021.104536.

[8] Mitsubishi Jukogyo KK. High strength, heat resisting steel welding electrode for welding boilers for power generation and pressurised chemical containers-consists of carbon, silicon, manganese, phosphorous, sulphur, chromium, nickel, molybdenum, vanadium, tungsten, niobium, rhenium, aluminium, boron and nitrogen at predetermined weight percentage. Japanese, 3426880-B2. 2003-07-14.

[9] Kobe Steel Ltd. Weld metal for high chromium ferritic heat-resistant steel used in pipes of boilers in electric power generation plant-has predetermined composition containing fixed ratio of niobium against vanadium in sodium chloride type carbonitride precipitated after stress relaxation process after welding. Japanese, 3527640-B2. 2004-05-17.

[10] Coleman KK, Gandy DW, Viswanathan R, Newell Jr, William F. Weld filler composition for use in welding steel pieces with different alloy content, such as low alloy ferritic steel and high alloy ferritic steel, comprises nickel, iron, chromium, niobium, carbon, manganese, molybdenum, and silicon. United States, 2005247763-A1. 2005-11-10.

[11] Kobe Steel Ltd. Wire for gas shielded arc welding of low-alloy heat-resistant steel, has flux coating which contains sodium, potassium and lithium compounds, titanium and metal fluoride. Japanese, 3815984-B2. 2006-08-30.

[12] Zhao L, Liang J, Zhong QP, Yang C, Sun B, Du JF. Numerical simulation on the effect of welding parameters on welding residual stresses in T92/S30432 dissimilar welded pipe. *Adv Eng Softw*, 2014, 68: 70-79. DOI: 10.1016/j.advengsoft.2013.12.004.

[13] Wu ZQ, Zhang X, Song XG, Ma CY, Qi YC, Chen X. Microstructure and properties of welded joint for T92 ferritic heat-resistant steel. *J Alloys Compd*, 2017: 140523. Doi.org/10.1016/j.jallcom.2017.01.156.

[14] Wang X, Wang X, Niu XG, Xiao DM, Hu XL. Application of nonlinear ultrasonic technique to characterize the creep damage in ASME T92 steel welded joints. *NDT & E Int*, 2018, 98: 8-16. DOI: 10.1016/j.ndteint.2018.04.006.

[15] Wang X, Wang X, Zhang YL, Wang C, Li Y, Huang QS. Microstructure and creep fracture behavior in HR3C/T92 dissimilar steel welds[J]. *Mater Sci Eng*, 2021, 799: 140128. DOI: 10.1016/j.msea.2020.140128.

[16] Zhang X, Qi YC. Comparative study of different welding wires on T92 welding joints. *Philos Mag Lett*, 2018, 9(4): 133-138. DOI: 10.1080/09500839.2018.1489151.

[17] Shanmugarajan B, Sathiya P, Buvanashekaran G. Mechanical and metallurgical properties of autogenous laser welded P92 material. *J Manuf Process*, 2016, 24(1): 11-18. DOI: 10.1016/j.jmapro.2016.07.003.

[18] Sklenička V, Kuchařová K, Svobodová M, Kvapilová M, Král P, Horváth L. Creep properties in similar weld joint of a thick-walled P92 steel pipe. *Mater Charact*, 2016, 119: 1-12. DOI: 10.1016/j.matchar.2016.06.033.

[19] Sirohi S, Pandey C, Goyal A. Role of heat-treatment and filler on structure-property relationship of dissimilar welded joint of P22 and F69 steel. *Fusion Eng Des*, 2020, 159: 111935. DOI: 10.1016/j.fusengdes.2020.111935.

Received 2021-08-11
Accepted 2022-10-28